Editors' Suggestion

Quantum diamond microscope for narrowband magnetic imaging with high spatial and spectral resolution

Zechuan Yin,[1,2] Jiashen Tang,[2,3] Connor A. Hart,[1,2] John W. Blanchard,[1,2] Xinyan Xiang,[2] Saipriya Satyajit,[2,3] Smriti Bhalerao,[2,4] Tao Tao,[2,3] Stephen J. DeVience,[2] and Ronald L. Walsworth[1,2,3,*]

[1] *Department of Electrical Engineering and Computer Science, University of Maryland, College Park, Maryland 20742, USA*

[2] *Quantum Technology Center, University of Maryland, College Park, Maryland 20742, USA*

[3] *Department of Physics, University of Maryland, College Park, Maryland 20742, USA*

[4] *Fischell Department of Bioengineering, University of Maryland, College Park, Maryland 20742, USA*

(Received 16 July 2024; revised 6 October 2024; accepted 18 October 2024; published 18 November 2024)

The quantum diamond microscope (QDM) is a recently developed technology for near-field imaging of magnetic fields with micron-scale spatial resolution, under ambient conditions. In the present work, we integrate a QDM with a narrowband measurement protocol and a lock-in camera, and we demonstrate imaging of radio-frequency (rf) magnetic field patterns produced by microcoils, with a spectral resolution of approximately 1 Hz. This rf QDM provides multifrequency imaging with a central detection frequency that is easily tunable over the megahertz scale, allowing spatial discrimination of both crowded spectral peaks and spectrally well-separated signals. The present instrument has a spatial resolution of approximately 2 μm, a field of view of approximately 300 × 300 μm^2, and a per-pixel sensitivity to narrowband fields of about 1 nT $Hz^{-1/2}$. Spatial noise can be reduced to the picotesla scale by signal averaging and/or spatial binning. The rf QDM enables simultaneous imaging of the amplitude, frequency, and phase of narrowband magnetic field patterns at the micron scale, with potential applications in real-space NMR imaging, ac susceptibility mapping, impedance tomography, analysis of electronic circuits, and spatial eddy-current-based inspection.

DOI: 10.1103/PhysRevApplied.22.054050

I. INTRODUCTION

Nitrogen-vacancy (N-V) centers in diamond are robust and sensitive detectors of magnetic fields, among other physical quantities [1,2]. In particular, the quantum diamond microscope (QDM), utilizing a dense, micron-scale near-surface layer of N-V centers in a diamond substrate, is a versatile platform for near-field magnetic field imaging, with diverse applications across the physical and life sciences [3]. To date, QDMs have mostly been used to image patterns of static or broadband magnetic fields, though narrowband measurements have also been performed, e.g., for real-space NMR imaging [4], ac magnetic susceptibility mapping [5], eddy current imaging [6], and phase-sensitive imaging of a narrowband signal produced by a stripline wire [7]. However, the CCD-camera-based measurements used in most QDMs to date have typically been slow due to a low frame rate and long exposure time, compared to single-channel measurements using a photodiode and digitizer, restricting the measurement bandwidth and temporal resolution. Moreover, the long exposure time of a CCD camera leads to low N-V spin-state optical contrast and a limited ability to mitigate broadband laser intensity noise, both of which result in reduced magnetic signal sensitivity [2]. Fortunately, the development of QDMs utilizing high-speed lock-in cameras provides a platform to acquire magnetic images at a faster rate, while applying phase modulation to increase the signal-to-noise ratio (SNR). In a recent demonstration [8], broadband magnetic imaging using Ramsey interferometry and a lock-in camera was realized, with submillisecond temporal resolution, micron-scale spatial resolution, and nanotesla-scale per-pixel sensitivity.

Here, we demonstrate narrowband magnetic imaging protocols, integrated with a QDM using a lock-in camera, and capable of high spectral and spatial resolution measurements of patterns of near-field radio-frequency (rf) signals. Beginning with dynamical decoupling sequences, we image in-phase, multifrequency subnanotesla rf signals (about 1 MHz) produced by spiral-shaped microcoils [Fig. 1(a)], and find good agreement with numerical

*Contact author: walsworth@umd.edu

 © 2024 American Physical Society

simulations. This rf QDM operates under ambient conditions and provides lateral spatial resolution of approximately 2 μm, a field of view (FOV) of approximately $300 \times 300\ \mu m^2$, and a per-pixel sensitivity to narrowband fields of about 1 $nT\,Hz^{-1/2}$. The central detection frequency can be easily tuned over several orders of magnitude by simple adjustments to the N-V measurement protocol. We also show that rf QDM measurements have good temporal stability by averaging down the spatial magnetic noise background to a few picotesla after 1 h. Subsequently, we apply the coherently averaged synchronous readout (CASR) [9] protocol, enabling simultaneous acquisition of amplitude and phase images of multifrequency rf signals with a 250-Hz spectral window and single-hertz resolution. Given the current performance of the rf QDM, we evaluate its feasibility for real-space N-V-NMR imaging of samples placed on the diamond imager chip, estimating the required acquisition times for imaging both thermally polarized and hyperpolarized NMR signals with various spatial resolutions. Notably, our approach is applicable to other quantum sensors, such as spin defects in silicon carbide (SiC) [10–12] and hexagonal boron nitride (h-BN) [13,14], thus providing a benchmark for narrowband magnetic imaging based on dynamical decoupling with any spin sensor.

II. EXPERIMENTAL METHODS

The present study employs a custom-built QDM utilizing a CVD-grown diamond plate [Fig. 1(a)] with a nitrogen-doped surface layer produced by Element Six, Ltd. Unless otherwise noted, measurements and simulations in the main text are for a diamond with a 10-μm layer [N-$V \approx 2.7$ ppm]. Results for a diamond with a 1.7-μm layer with the same N-V concentration, as well as other rf QDM technical details, are reported in Appendix C. The negatively charged N-V^- center (otherwise referred to as the N-V center throughout this paper) possesses a triplet ground-state spin [Fig. 1(b)] that can be optically initialized and read out. In this work, 532-nm green laser light is coupled into a polished side facet of the diamond plate, undergoing total internal reflection and illuminating an approximate (400×600)-μm^2 region of the N-V-doped layer. A nominal 22-mT bias magnetic field is aligned to one of the four N-V ensemble orientations in diamond for sensing the projection of signal rf magnetic fields along that particular sensing N-V orientation (defined as the z axis). The spin-state-dependent N-V fluorescence is subsequently collected with an objective (20×/0.75 NA Nikon) and imaged with a lock-in camera (Heliotis heliCam C3) capable of external frame rates up to 3.8 kHz.

An arbitrary waveform generator (AWG) is used to control the experimental apparatus, including direct synthesis of the microwave (MW) pulses that drive transitions between the N-V $m_s = 0$ and $m_s = +1$ sublevels

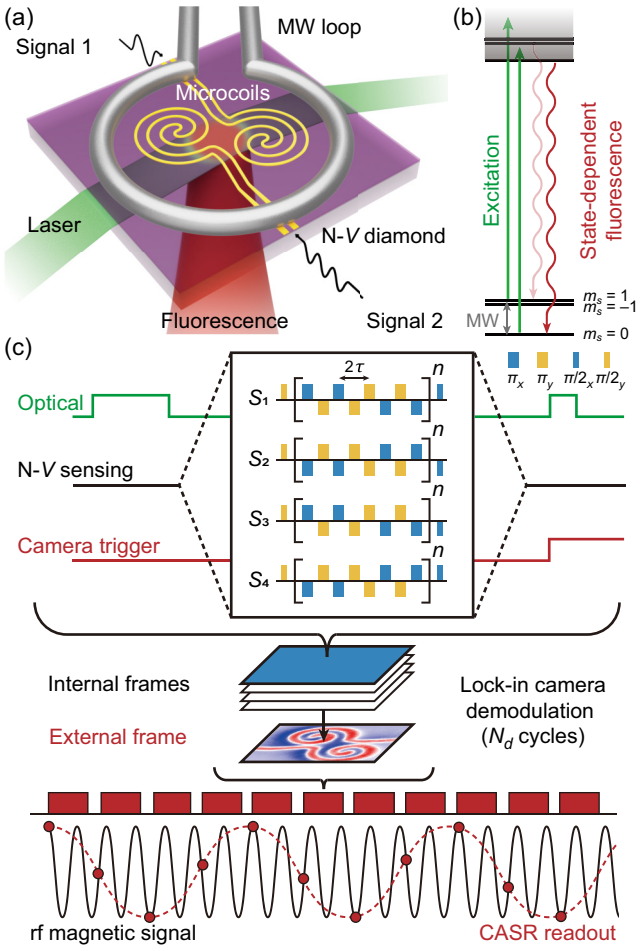


FIG. 1. (a) Wide-field imaging of near-field patterns of narrowband magnetic fields utilizing a quantum diamond microscope (QDM) operating under ambient conditions. rf test signals are applied to microcoils to produce distinct magnetic field patterns across the N-V-diamond surface. Laser and microwave (MW) fields are employed for N-V electronic spin manipulation, with spin-state population readout through fluorescence detection. (b) N-V energy-level diagram. The N-V^- center in diamond exhibits spin-dependent fluorescence with triplet ground-state spin transitions. (c) rf magnetic field imaging protocol with a lock-in camera. Within one camera demodulation cycle, four exposures occur, with phase-modulated XY8-n sequences applied to N-V spins to generate internal in-phase and quadrature frames. After N_d cycles (i.e., $2N_d$ total internal frames), an external frame of the rf magnetic field image is obtained. The CASR protocol comprises interspersed blocks of single external frame measurements (red boxes) with a frame rate of f_{SR}. The rf magnetic signal (black curve) with frequency f_s is sampled via CASR readout (red dashed curve) at an alias frequency $f_s - mf_{SR}$, where m is the integer closest to f_s/f_{SR}.

[Fig. 1(b)]. The AWG marker channels synchronize the camera acquisition and gating of an acousto-optic modulator used to generate optical pulses exciting the N-V layer. In addition, the AWG produces independent rf test signals applied to two spiral-shaped microcoils on the

N-V-diamond surface, which provide spatially varying magnetic field patterns across the FOV.

For each imaging pixel, the local rf magnetic fields generated by the microcoils can be measured using a dynamical decoupling protocol (XY8-n), where the net phase acquired by the N-V electronic spin due to the oscillating field is mapped onto a difference in the ground-state spin population by a final $\pi/2$ pulse prior to readout. Four different XY8-n sequences, comprising a single demodulation cycle, are interwoven between exposures of the lock-in camera, as depicted in Fig. 1(c), and the corresponding N-V fluorescence signals are labeled as $S_{1,2,3,4}$. By controlling the phase of the final $\pi/2$ pulse, one can enhance the readout signal contrast and subtract broadband laser intensity noise by leveraging the in-pixel lock-in camera demodulation. In each cycle and for every pixel, the camera generates an in-phase (I) signal (i.e., internal I frame) by analog subtraction of the third exposure from the first, and a quadrature (Q) signal (i.e., internal Q frame) as the difference between the second and fourth exposures. The accumulated difference signals after N_d demodulation cycles are digitized to produce external I and Q frames, which are stored in an on-board, memory buffer. Finally, since each I and Q frame pair contains the same information due to the specific phase alternation pattern employed, they are summed to form one external frame of the readout signal after transfer to the host computer. Thus, there are $2N_d$ total internal frames for each external frame. For an applied rf test signal with $B_{\mathrm{rf}} = B_z \cos(2\pi f_s t + \phi_0)$, where B_z is the projection of the signal magnetic field amplitude on the N-V axis, f_s is the oscillation frequency, and ϕ_0 is the phase offset, the readout signal for each pixel of an external frame can be written as $S = N_d[(S_1 - S_3) - (S_2 - S_4)] = 4N_d S_a \sin(\kappa B_z \cos\phi_0)$, where S_a is the signal oscillation amplitude, $\kappa = 2\gamma N_\pi / f_s$ is a constant, $\gamma = 2\pi \times 28.024$ GHz/T [15] is the N-V electronic gyromagnetic ratio, and N_π is the π-pulse number in the XY8-n sequence. When sensing a small magnetic field shift ΔB_z, the change in N-V fluorescence readout is given by $\Delta S = 4N_d S_a \kappa \Delta B_z$. By calibrating the magnetometry slope of each pixel, the rf magnetic field image can be extracted from the fluorescence image, as shown in Appendix B.

The CASR protocol [9] is employed for simultaneous near-field imaging of the amplitude, frequency, and phase of rf signal patterns, with high spectral resolution (approximately 1 Hz). By recording consecutive lock-in camera external frames [Fig. 1(c)], the time-dependent rf magnetic field is captured by interspersed N-V spin-state readouts at a sampling rate of f_{SR}, equal to the external frame rate. Using the CASR protocol, an oscillating N-V fluorescence signal in the time domain is read out for each pixel. Applying a fast Fourier transform (FFT) yields frequency-domain CASR spectra for each pixel, centered at the alias frequency $f_s - mf_{\mathrm{SR}}$, with peak amplitude $S_{\mathrm{CASR}} = 4N_d(2\pi)^{3/2} S_a J_1(\kappa B_z)$ (see Appendix D for details), where $J_1(x)$ is the first-order Bessel function and m is the integer closest to f_s/f_{SR}. For the demonstrations presented here, we experimentally ensure that $\kappa B_z < 1$ such that the first-order Bessel function closely approximates a linear function, leading to $S_{\mathrm{CASR}} \propto B_z$.

III. RESULTS

A. In-phase rf magnetic imaging

To characterize the performance of the rf QDM, we begin by imaging narrowband magnetic fields with known phase. We simultaneously apply alternating current (ac) signals at 1 and 0.8 MHz, each with a peak value of 6.6 μA, to two separate microcoils on the N-V-diamond surface [Fig. 2(a)]. We first align the XY8-8 sensing sequence in phase with the 1-MHz signal by setting the π-pulse spacing to $\tau_1 = 0.5$ μs and sweep the test signal phase to obtain maximum signal. After a 1.2-s acquisition (200 camera external frames), we obtain an rf magnetic field amplitude image with a peak-to-peak difference of about 130 nT, revealing the near-field pattern generated by *only* the upper microcoil with SNR ≈ 50 [Fig. 2(b)]. Adjusting the spacing between XY8-8 π pulses ($\tau_2 = 0.625$ μs) to be in phase with the 0.8-MHz signal, we record the magnetic field pattern produced *only* by the lower microcoil. The rf QDM provides clean near-field images of either signal frequency, with no significant "crosstalk" between the simultaneously applied signal patterns, because the test signal frequencies are spectrally separated by more than the narrowband filter function of the sensing sequence [Fig. 2(c)]. The center frequency of the filter function is easily tunable, as it is determined by the spacing τ between pulses in the sensing sequence, while the bandwidth (spectral detection window) is determined by the number of repetitions, n, of the XY8-n sequence [16]. For the present demonstration, using an XY8-8 sensing sequence and signal frequencies of about 1 MHz, the filter function bandwidth is approximately 30 kHz. This demonstration illustrates the ability of the rf QDM to perform micron-scale spatial discrimination of spectrally well-separated narrowband signals.

In Fig. 2(b), the measured rf magnetic field distributions are compared to numerical simulations. We calculate the three-dimensional magnetic field generated by a static current of 6.6 μA constrained to the physical geometry of the spiral-shaped microcoils using finite element software [17]. Averaging the magnetic field at a 10-μm stand-off distance over the 10-μm N-V layer thickness and projecting the field vector onto the sensing N-V orientation, the simulated magnetic field images are consistent with measurements. To highlight the sensitivity and stability of the rf QDM, we reduce the amplitude of the two test signals to 26.4 nA. Following an acquisition time of 3600 s for each signal frequency, we obtain images of the in-phase narrowband magnetic field amplitude generated by each microcoil, with a peak-to-peak difference of about 500 pT

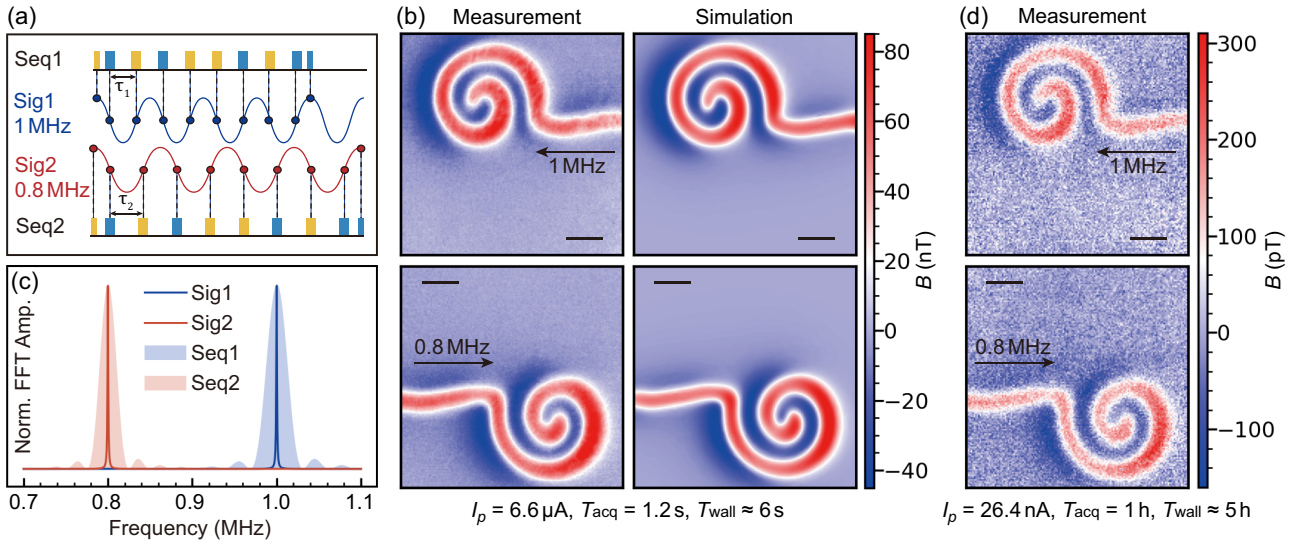


FIG. 2. rf QDM imaging of narrowband, multifrequency magnetic fields of known phase, using a dynamical decoupling (XY8-8) protocol. (a) Simultaneously, a 1-MHz alternating current (Sig1) is applied to the upper microcoil on the N-V-diamond surface [Fig. 1(a)], and a 0.8-MHz current (Sig2) is applied to the lower microcoil. By adjusting the spacing between π pulses, the dynamical decoupling sequence becomes sensitive to different signal frequencies. The diagram presented here illustrates simple XY8 sequences, while in the experiment, an XY8-8 sequence with phase modulation is employed, as depicted in Fig. 1(c). (b) Comparison of measured (left) and simulated (right) magnetic field images resulting from alternating currents with a peak value of 6.6 μA. After averaging over 1.2 s (for each signal frequency), the experimental images exhibit an SNR of approximately 50, calculated as the ratio of the maximum signal contrast to the standard deviation within a quarter of the FOV, excluding the signal. By adjusting the π-pulse spacing τ, the XY8-8 sensing sequence can be synchronized with either Sig1 or Sig2, enabling imaging of rf magnetic field patterns generated by each microcoil individually, with no observable "crosstalk" in the images between the simultaneously applied signals. Because of the data transfer time from the camera to the computer, the wall time of this experiment is approximately 6 s. (c) Calculated FFT spectra of the two signals applied to the microcoils (blue and red solid lines), and filter functions of the XY8-8 sequences used for spectrally selective rf QDM measurements (shaded blue and red regions). Both the signal and filter function amplitudes are normalized. A 10-Hz linewidth is added to the signal peaks for better visualization. Here, we only show the first-order filter function; the XY8 sequences can also sense higher-order odd harmonics. (d) Demonstration of sub-nanotesla-scale rf magnetic imaging. By reducing the peak value of the applied alternating currents to 26.4 nA, images are obtained of the rf magnetic field patterns from Sig1 and Sig2, with an SNR of about 15 after 1 h of signal averaging (for each signal frequency). All scale bars correspond to 50 μm in this figure. The colorbars in (b) and (d) are not centered around zero because of asymmetry in the projection of the rf signal magnetic field amplitude on the sensing N-V axis.

and SNR ≈ 15 [Fig. 2(d)]. Note that a machine learning approach has recently been applied to the inverse problem of reconstructing the current distribution from QDM magnetic field images [18].

B. rf magnetic imaging performance

With a 20× magnification objective and 39.6-μm camera pixel size, the rf QDM has a 2-μm lateral optical resolution, corresponding to the size of a single pixel in the magnetic images [Figs. 2(b) and 2(d)]. For the diamond with a 10-μm N-V layer diamond, each sensing voxel is an approximate $(2 \times 2 \times 10)$-μm^3 region; in this case, a single camera pixel can collect fluorescence from adjacent N-V sensing voxels, resulting in QDM-rf spatial resolution greater than 2 μm. For the 1.7-μm N-V layer diamond, the QDM-rf spatial resolution is approximately 2 μm (see Appendix C). For the dynamical-decoupling-based experiments discussed above, we vary the number of XY8 sequences and measure the narrowband sensitivity of each pixel across the FOV for a 1-MHz signal frequency, as shown in Appendix F. The optimized sequence is determined to be XY8-8, with a median per-pixel sensitivity of 0.93(1) nT Hz$^{-1/2}$. Given a sensing voxel volume of approximately 40 μm^3 for the 10-μm N-V layer diamond, the volume-normalized sensitivity is about 6 nT Hz$^{-1/2}$ μm$^{3/2}$, which is comparable to state-of-the-art ensemble N-V sensitivity using XY8 sequences and photodiode (nonimaging) measurements [19]. We estimate the contribution of two per-pixel noise sources: photon shot noise of approximately 0.3 nT Hz$^{-1/2}$ and camera quantization noise of approximately 0.86 nT Hz$^{-1/2}$, indicating that the present rf QDM's narrowband sensitivity is limited by the camera. A similar performance analysis is presented in Appendix F for the rf QDM using the 1.7-μm N-V layer diamond.

In addition to per-pixel sensitivity, spatial noise (due to pixel-to-pixel variance from the camera and spatially

varying diamond crystal stress) is another significant parameter for evaluating rf QDM performance. To characterize the spatial noise, we conduct single-frame measurements without an applied rf magnetic signal. At a given narrowband detection frequency, the spatial noise floor of an rf QDM image, σ_{Spatial}, is defined as the pixel-to-pixel standard deviation of the measured in-phase magnetic field amplitude at the detection frequency, determined across the entire FOV, and is inversely proportional to the square root of the averaging frame number. During magnetic imaging, a trade-off arises between spatial resolution and spatial noise. One strategy to mitigate spatial noise is to bin pixels, i.e., group adjacent pixels together to create "superpixels," and thereby effectively reduce the overall spatial noise in the image, albeit with coarser spatial resolution. For applications where the highest spatial resolution of the rf QDM is not required, averaging over the space domain rather than the time domain allows for shorter acquisition times with similar SNR. We demonstrate this approach for 5×5 binned superpixels of size 10 μm. With no signal applied to the microcoils, we observe $\sigma_{\text{Spatial}} \propto T_{\text{acq}}^{-1/2}$ for rf QDM images and a 1-MHz detection frequency, where T_{acq} is the data acquisition time for both 2-μm (unbinned) pixels and 10-μm superpixels [Fig. 3(a)]. This behavior indicates that the rf QDM's spatial magnetic noise can be suppressed with time averaging out to hour timescales. The spatial noise floor of a single frame with 1.2-s acquisition time and 10-μm superpixel resolution is similar to that of a 30-s average of multiple frames with 2-μm single-pixel resolution. With 10-μm superpixel spatial resolution and 1-h acquisition time, the rf QDM can average the spatial noise background down to 7.1(1) pT [Fig. 3(b)]. The median per-pixel narrowband sensitivity for a 10-μm superpixel is also improved to 0.18(1) nT $\text{Hz}^{-1/2}$.

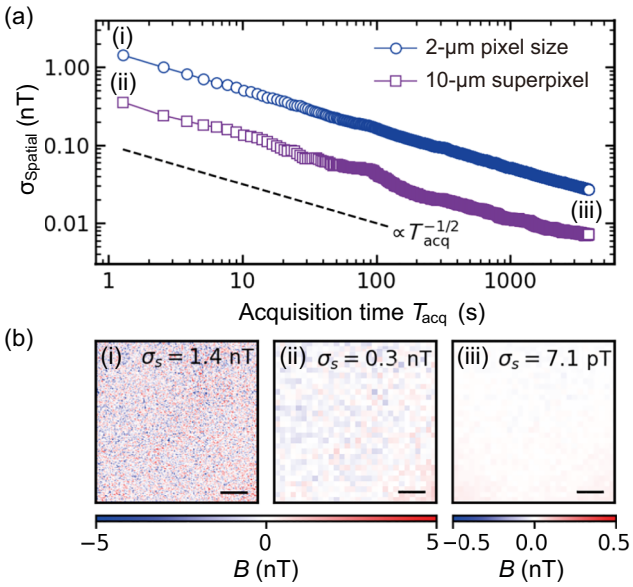


FIG. 3. Suppressing spatial noise in rf QDM magnetic images by averaging over time and/or space. (a) Measured magnetic spatial noise floor σ_{Spatial} with no rf signal applied to the microcoils and a 1-MHz detection frequency, as a function of data acquisition time T_{acq}, for 2-μm single-pixel resolution and 10-μm (binned) superpixel resolution. A dashed black line depicts the power-law scaling behavior $\propto T_{\text{acq}}^{-1/2}$ as a guide to the eye. (b) Example rf QDM magnetic images of the noise background and resulting σ_{Spatial}: (i) 2-μm single-pixel resolution with $T_{\text{acq}} =$ 1.2 s; (ii) 10-μm superpixel resolution with $T_{\text{acq}} = 1.2$ s; (iii) 10-μm superpixel resolution with $T_{\text{acq}} = 3600$ s. Corresponding values for σ_{Spatial} are labeled in (a). All scale bars correspond to 50 μm in this image. The magnetic noise is distributed randomly without significant spatial correlation. The comparison between (i) and (ii) shows that spatial noise can be averaged over space, while the comparison between (ii) and (iii) illustrates an average over time. Note that the frame rate of the lock-in camera is constant in all measurements.

C. Simultaneous amplitude and phase imaging

Next, we implement the CASR protocol in the rf QDM, and simultaneously image the amplitude and phase of a multifrequency rf magnetic field, with spectral resolution of approximately 1 Hz, as shown in Fig. 4. For these demonstration measurements, we simultaneously apply a dual-tone alternating current $I_1 = I_p \cos[2\pi(f_0 + f_1)t + \theta_1] + I_p \cos[2\pi(f_0 + f_3)t + \theta_3]$ to the lower microcoil, and a single-tone current $I_2 = I_p \cos[2\pi(f_0 + f_2)t + \theta_2]$ to the upper microcoil. Here, $f_0 = 1$ MHz is the carrier frequency; $f_{1,2,3}$ are 65, 125, and 185 Hz, respectively; and $\theta_{1,2,3}$ are arbitrary phase offsets of each frequency component, which are fixed during the measurements. The current peak value of $I_p = 3.3$ μA is half that of the in-phase signals used in the above results [Fig. 2(b)], with an estimated peak rf magnetic field amplitude less than 40 nT, which is in the linear response range of the measurement. The lock-in camera frame rate is set to $f_{\text{SR}} = 500$ Hz with eight demodulation cycles per frame. After 1 s of measurement, a series of N-V fluorescence images are acquired [Fig. 1(c)], which gives the rf magnetic field change in the time domain, sampled at the CASR alias frequency. We repeat the measurement 100 times to average down the noise floor, then perform an FFT to the measured time-dependent fluorescence change of each pixel. Finally, we normalize the CASR signal amplitude to the steady-state N-V fluorescence for each pixel (in the absence of any N-V spin-state modulation) to extract the magnetic field amplitude images of each frequency component, as described in Appendix D.

Three test pixels are selected to illustrate the CASR amplitude imaging results [Figs. 4(a) and 4(b)]. For pixel P_1, which is located at the upper microcoil, only one frequency peak at f_2 is observed in the CASR spectrum. Pixel P_3, located at the lower microcoil, exhibits two frequency components in its CASR spectrum, corresponding

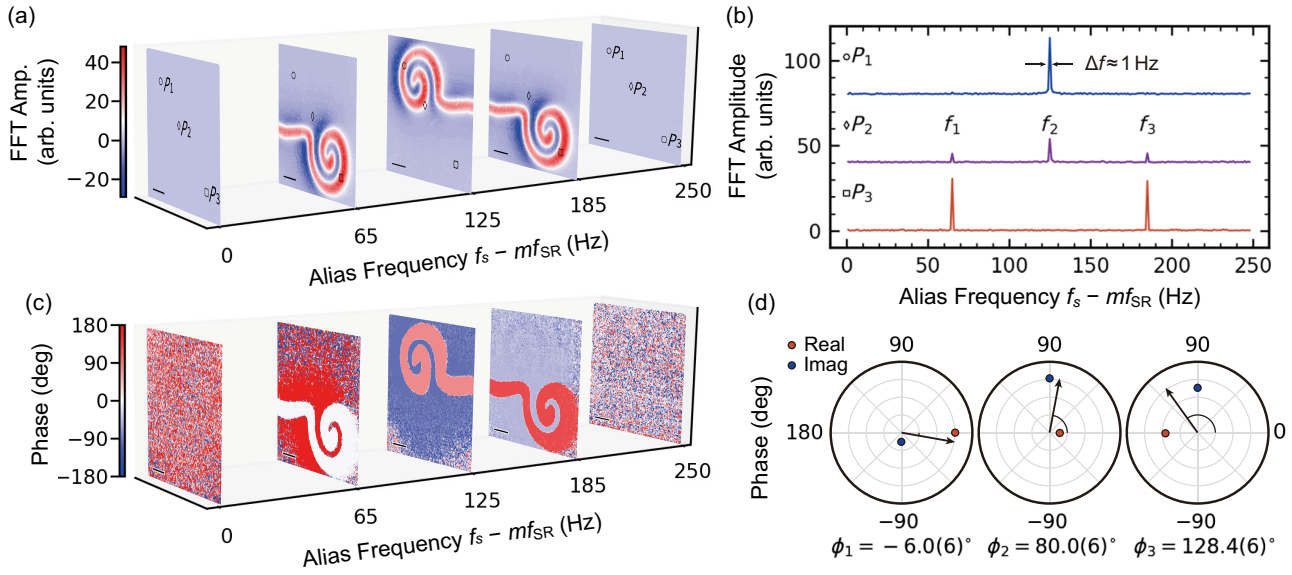


FIG. 4. rf QDM imaging of arbitrary phase, multifrequency magnetic fields using the CASR protocol. As described in the main text, a single-tone alternating current (1 MHz + 125 Hz) is applied to the upper microcoil, and a two-tone current (1 MHz + 65 Hz and 1 MHz + 185 Hz) is simultaneously applied to the lower microcoil. Both currents have peak amplitude $I_p = 3.3$ μA. The phases of each signal frequency component (tone) are arbitrary but fixed during the measurements. Total image acquisition time is 200 s. (a) CASR images of rf magnetic field amplitudes at each signal frequency component, as well as at alias frequencies (1 and 250 Hz) far from any signal tone. The imaged arbitrary phase magnetic field amplitudes have an SNR of approximately 70 [calculated with the same method as for Fig. 2(b)] for each signal frequency component, and exhibit good agreement with images of in-phase signals shown in Fig. 2(b). The colorbar is not centered around zero because of asymmetry in the projection of the rf magnetic field amplitude on the sensing N-V axis. (b) CASR spectra (FFT) of three test pixels $P_{1,2,3}$ with positions labeled in (a). Peaks corresponding to three frequency components $f_{1,2,3}$ are clearly illustrated in the spectra, with peak heights proportional to the rf magnetic field amplitude. Linewidths of all spectral peaks are approximately 1 Hz. Amplitude offsets are added to the spectra of $P_{1,2}$ for a better visualization. (c) CASR images of rf magnetic field phases at each signal frequency component, as well as at alias frequencies far from any signal tone (1 and 250 Hz). Noisy phase distributions in no-signal regions are attributed to the ratio of near-zero real and imaginary amplitudes of the CASR FFT. (d) Polar plots illustrate the phases of each signal frequency component, derived from CASR measurements. Here ϕ_1 and ϕ_3 are determined from the real and imaginary parts of the FFT of pixel P_3, and ϕ_2 is determined from P_1. Red and blue dots represent the real and imaginary amplitudes of the associated FFT spectra, respectively, while black arrows indicate the absolute value of the amplitude as shown in (a). Grids are depicted as circles with a step size equivalent to the radius of ten arbitrary units of FFT amplitude. All scale bars in (a) and (c) correspond to 50 μm.

to f_1 and f_3. The central pixel P_2, located between the two microcoils, exhibits frequency components from both sources, with reduced amplitude. In all cases, the linewidth of CASR spectral peaks $\Delta f \approx 1$ Hz. From the CASR spectra of each pixel, we can generate magnetic field amplitude images for each frequency component within the measurement bandwidth, as shown in Fig. 4(a) for five different example frequencies. The illustration of CASR amplitude images at frequencies $f_{1,2,3}$ provides insight into the rf magnetic field patterns generated by both microcoils, consistent with the in-phase magnetic field images and simulation results presented in Fig. 2(b).

The CASR protocol also enables simultaneous magnetic field phase imaging for each frequency component within the measurement bandwidth. The phases of each measured frequency component, $\phi_{1,2,3}$, are dependent on the phases, $\theta_{1,2,3}$, of the input test signals, the impedance of the microcoils, and the time delay between the current signal and the CASR sensing sequence. All of these parameters are fixed during measurement, which provides arbitrary but stable phases for the imaged rf magnetic field patterns. When extracting the CASR amplitude from time-domain N-V fluorescence measurements, it is essential to consider the phase-dependent real and imaginary components of the CASR FFT spectra. The root mean square of these components yields the amplitude, while the phase can be extracted from the ratio. Based on the measured real and imaginary components of the CASR spectra at locations P_1 and P_3, we determine phases $\phi_{1,2,3}$ for each signal frequency component with an accuracy of 0.6° calculated from the noise floor in Fig. 4(b). Repeating the same phase calculation for each pixel across the FOV, we obtain phase images at each frequency step of the CASR spectra, as shown in Fig. 4(c). Further details are discussed in Appendix E.

IV. DISCUSSION

A promising application of the rf QDM is micron-scale real-space NMR imaging. The rf QDM's hertz-scale spectral resolution will enable micron-scale spatial identification of chemical shifts and J couplings in samples on the diamond surface [9]—key spectral identifiers of molecular structure that are critical to NMR applications in chemistry, life science, and materials research. Based on the results from previous N-V-NMR research [9,20], we estimate a spatial noise threshold of 50 pT for resolvable micron-scale NMR images with SNR > 1 for a thermally polarized sample in an external (bias) magnetic field about 0.1 T, and a spatial noise threshold of 10 nT if using dynamic nuclear polarization (DNP) of the sample. Assuming the current rf QDM performance, an acquisition time around 40 s is required for a thermally polarized sample to surpass this threshold with spatial resolution of 10 μm, whereas DNP hyperpolarization would allow the threshold to be passed in about 30 ms with 2-μm spatial resolution [Fig. 3(a)]. (Other hyperpolarization techniques can provide even greater nuclear spin polarization, and N-V-NMR signal amplitude [21], albeit with operation typically limited to lower bias fields.) With the millisecond-scale time resolution of the rf QDM's lock-in camera, it may thus be possible to image real-time NMR dynamics in micron-scale samples, including chemical processes in living systems at the cellular scale and samples within microfluidic structures [22]. To demonstrate the ability of the rf QDM to spatially discriminate narrowband signals that are spectrally crowded (i.e., differ in frequency by a few tens of hertz, as in many NMR signals of interest), we show example CASR images of weighted frequency and phase from the two microcoils with 60-Hz offset in their signals [around a 1-MHz carrier frequency; Fig. 5]. The near-field rf signals produced by the two microcoils are clearly distinguished at the micron scale by their different frequencies and phases. Similar weighted frequency (or phase) N-V-NMR images could allow detailed spatial monitoring of chemical concentrations in samples of interest.

In this work, the amplitude of rf magnetic signals is held constant during measurements. However, it is worth noting that rf QDM measurement protocols are applicable to signals with decay envelopes, such as free-inductive decay in NMR experiments. A time-domain decay envelope manifests as finite FFT peak linewidths in the CASR spectrum of each pixel, yielding spatial information from both the imaged signal frequencies and linewidths. This capability of real-space imaged N-V-NMR spectroscopy holds promise for applications involving micron-scale samples with spatially varying concentrations and local environments of NMR-detectable nuclear species. Furthermore, technical advances in the lock-in camera frame rate and storage capacity can lead to corresponding improvements in the sensing bandwidth and spectral resolution for micron-scale NMR and other applications. In addition, the rf QDM should be compatible with magnetic field gradients applied to the N-V spins [23,24], potentially allowing combined Fourier and real-space NMR imaging with nanoscale spatial resolution and the FOV approaching a millimeter.

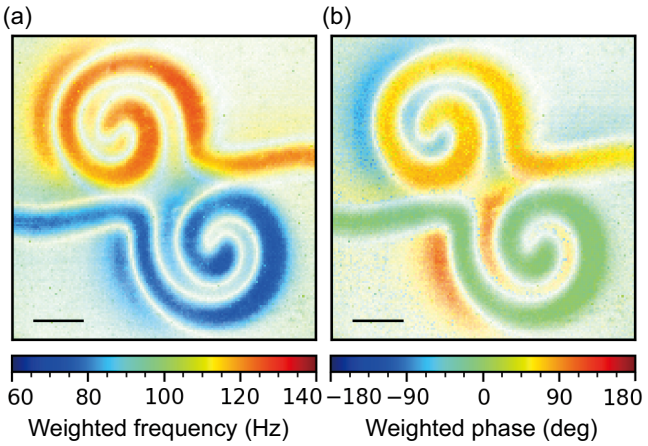


FIG. 5. rf QDM CASR imaging of weighted frequency and phase of magnetic signals generated by the two microcoils for the same experimental conditions and CASR imaging protocol as in Fig. 4. (a) The weighted frequency $f_w = \int f\, S_{\mathrm{CASR}}\, df \,/ \int S_{\mathrm{CASR}}\, df$. A transparency mask, based on the integral of the CASR amplitude of each pixel, is applied to the image data to filter out the no-signal region for better visualization. The colorbar indicates the frequency integration range, which in this example includes f_1 and f_2, but excludes f_3. The near-field, micron-scale spatial distribution of the two included frequency components is clearly illustrated in the image. (b) Weighted phase image of the rf magnetic signal generated by the two microcoils. The weighted phase $\phi_w = \int \phi\, S_{\mathrm{CASR}}\, df \,/ \int S_{\mathrm{CASR}}\, df$. The transparency mask and integration range are the same as in (a). The spatial distribution of $\phi_1 = -6^\circ$ and $\phi_2 = 80^\circ$ is clearly illustrated. The approximate 180° phase-shifted signal outside each spiral is due to the opposite directions of the rf magnetic field generated by the microcoils. All scale bars correspond to 50 μm in this image.

We also highlight other promising applications of the rf QDM. Previous work demonstrated single-channel measurement of the ac susceptibility of two-dimensional magnetic materials using N-V centers and XY8 sequences [25]. The rf QDM will allow micron-scale mapping of the spatial distribution of ac susceptibility, which could serve as an important calibration process for material science investigations. The rf QDM can also be applied to imaging inductive eddy currents in electrical conductors [26]. By simultaneously imaging the amplitude and phase of the inductive ac magnetic signal, the rf QDM could provide higher spatial resolution and better sensitivity than conventional techniques for eddy current inspection. For integrated circuits and other micron-scale electronics, the

rf QDM may be useful for failure analysis [27,28] and hardware Trojan detection [29]. Mapping circuit magnetic field activity across various operating frequencies, the rf QDM could provide complementary information to static field images [30,31] and other electromagnetic properties. Additionally, the rf QDM can be applied to impedance tomography, which is widely used in biological science [32]. Instead of using arrays of coplanar electrodes to detect the spatial distribution of modulated stimulation currents in living cells and tissue—which is invasive and only provides a limited set of point measurements—the rf QDM may provide a noninvasive direct image of the current amplitude and phase, with full spatial coverage across the FOV.

In summary, we characterize the performance of a lock-in-camera-based QDM for narrowband magnetic field imaging, and demonstrate imaging protocols for multifrequency wide-field imaging of near-field patterns of rf signals generated by fabricated microcoils, with approximately 1-Hz spectral resolution. This rf QDM operates under ambient conditions and provides per-pixel sensitivity to narrowband fields of about 1 nT $\mathrm{Hz}^{-1/2}$ with approximately 2-μm spatial resolution across a (300×300)-$\mu\mathrm{m}^2$ FOV. With temporal averaging and spatial binning, the spatial noise floor is reduced to the picotesla scale, similar to the expected signals from potential applications of real-space N-V-NMR imaging using thermally polarized samples. The rf QDM simultaneously captures the micron-scale spatial distribution of the amplitude, frequency, and phase of rf magnetic fields, also paving the way for other application areas such as ac susceptibility imaging, eddy current inspection, assessment of electronic circuits, and impedance tomography.

Note that, for the results presented here, the rf magnetic field amplitude images depict the projected value on the sensing N-V orientation. However, as there are four N-V orientations in diamond, the rf QDM should be applicable to imaging of the rf magnetic field vector [33]. This capability, to be demonstrated in future work, could also allow the correction of image artifacts related to variation of the rf magnetic field direction across the finite N-V layer. In addition, the present rf QDM is limited to signal frequencies < 10 MHz by technical constraints on the N-V Rabi frequency. Future advances in delivered MW signal strength (and hence increased N-V Rabi frequency), or the application of a quantum frequency mixing protocol [34], will allow imaging of higher signal frequencies (from about 10 MHz to the gigahertz range). We also note that the rf QDM is compatible with narrowband sensing protocols that provide improved sensitivity compared to the XY8 sequence, e.g., DROID-60 [35,36] and quantum logic enhanced repetitive readout [19]. However, these protocols typically have increased complexity, resulting in a longer sensing time. Currently, due to limitations imposed by the memory of the rf QDM's lock-in camera, employing such protocols would reduce the frame rate and available measurement time, leading to a reduced spectral detection window for CASR imaging. Improvements in camera technology and data processing algorithms may help alleviate these limitations, further enhancing rf QDM performance for narrowband magnetic field imaging.

ACKNOWLEDGMENTS

We acknowledge the Maryland NanoCenter and its FabLab for providing instruments and assistance to fabricate the microwave waveguide and microcoils. This work is supported by, or in part by, the U.S. Army Research Laboratory under Contract No. W911NF1920181; the U.S. Army Research Office under Grant No. W911NF2120110; the U.S. Air Force Office of Scientific Research under Grant No. FA9550-22-1-0312; the Gordon & Betty Moore Foundation under Grant No. 7797.01; and the University of Maryland Quantum Technology Center.

APPENDIX A: EXPERIMENTAL DETAILS

Two side-polished diamond samples are employed in this work: one contains a 10-μm-thick, ^{15}N-enriched CVD layer of N-V centers ($[\mathrm{N}] = 17$ ppm, $> 99.99\%$ ^{12}C), grown by Element Six Ltd. on a $(2 \times 2 \times 0.5)$-mm^3 high-purity diamond substrate, with postgrowth treatment via electron irradiation and annealing to increase the N-V concentration to 2.7 ppm; the other diamond sample contains a 1.7-μm-thick N-V layer with the other properties being the same.

A diode-pumped solid-state laser (Lighthouse Photonics, Sprout-H) is employed to generate a continuous-wave 532-nm laser beam. The laser beam is focused onto an acousto-optic modulator (AOM; Gooch & Housego, Model 3250-220) by an $f = 500$-mm spherical convex lens, and the first-order diffracted beam from the AOM is used for the experiments. To create optical pulses for N-V initialization and readout, the rf driver for the AOM is gated by a switch (Mini-Circuits, ZASWA-2-50DR+) that is controlled by transistor-transistor logic (TTL) pulses from the marker channel of an arbitrary waveform generator (AWG; Zurich Instruments, SHFSG). The first-order beam after the AOM is further shaped by an $f = 130$-mm cylindrical convex lens and an $f = 100$-mm spherical convex lens to produce an elliptical beam profile incident on a polished side surface of the diamond sample. Approximately 2.5 W of laser light enters the diamond and undergoes total internal reflection at the surface with the N-V layer, illuminating an area of about 400×600 $\mu\mathrm{m}^2$. N-V fluorescence (also commonly referred to as photoluminescence or PL) is collected by a $20 \times /0.75$ NA Nikon objective, and filtered by a 647-nm long-pass filter (Semrock) before projecting onto a photodiode (Thorlabs, PDA36A2) or a lock-in camera (Heliotis, heliCam C3). Photodiode

voltage measurements are acquired using a data acquisition system (DAQ) system (National Instruments, NI USB6259).

Microwave (MW) pulses for N-V spin control are generated by a signal channel of the same AWG used for generating TTL pulses. A fabricated 300-nm-thick, 800-μm inner diameter gold Ω-shaped coplanar waveguide delivers MW pulses to control the N-V electron spins, generating a homogeneous MW driving (Rabi frequency) region covering the FOV. The fabricated palladium spiral microcoils, used for generating spatial patterns of rf signals, have a trace width of 5 μm, span a (280 × 300)-μm^2 area, and have a thickness of 10 nm [Fig. 6(a)]. Palladium is used because of its relatively high resistance (e.g., compared to gold) in order to avoid large mutual inductance between the microcoils and the MW coil, which could degrade performance of the MW coil. The microcoils and MW loop are fabricated on a SiC wafer for mechanical support and heat dissipation. The diamond is glued to the surface of the MW loop with an estimated stand-off distance of 10 μm. To generate rf magnetic field patterns, multifrequency voltages produced by other signal channels of the AWG are applied to the microcoils to induce currents. An rf test coil, wound from 22 American Wire Gauge with 14 loops and a diameter of 50 mm, is placed on the top of the SiC wafer to generate test signals for magnetometry curve calibrations, as shown in Appendix B. A bias magnetic field of approximately 22 mT is provided by four pairs of temperature-compensated, permanent samarium cobalt ring magnets. Ring magnet pairs provide a more homogeneous bias magnetic field than cylinder-shaped magnets.

The size of a single camera pixel in the objective focal plane is determined using the known size of the microcoils and an optical image visualized using N-V fluorescence. The metallic surfaces of microcoil traces reflect the excitation laser and increase the local illumination intensity, resulting in greater N-V fluorescence with a pattern following the phantom structure, as shown in Fig. 6(b). The area occupied by each camera pixel corresponding to the focal plane is 2 × 2 μm^2, which agrees with the estimate using the magnification of the objective (20×) and the physical size of each pixel (39.6 × 39.6 μm^2), as reported by the camera manufacturer. A schematic of the experimental apparatus is shown in Fig. 6(c).

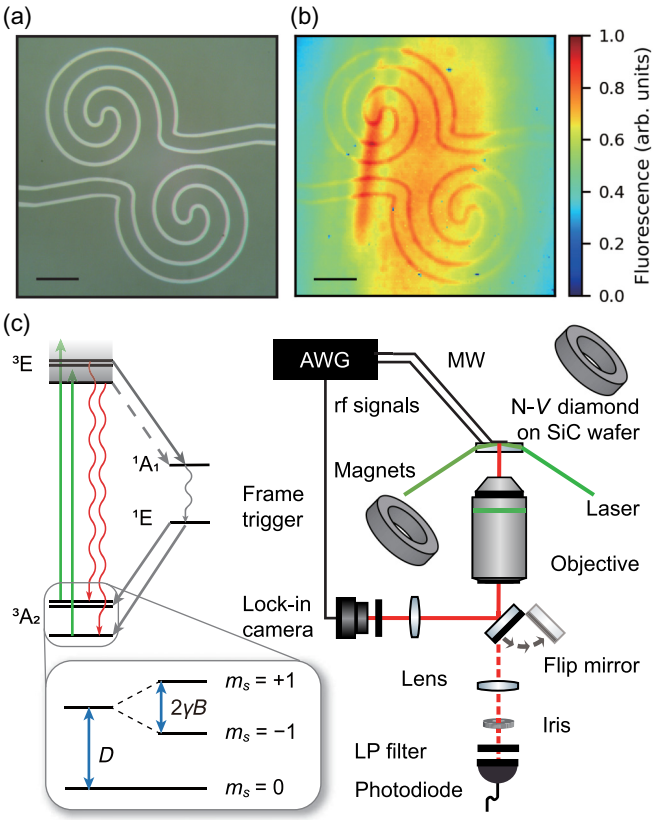


FIG. 6. (a) Optical image of the spiral-shaped microcoils with a stand-off distance of approximately 10 μm to the N-V layer. All scale bars correspond to 50 mm. (b) N-V fluorescence image under continuous-wave laser excitation illustrating the relative illumination of the N-V layer (i.e., beam shape) in the FOV. The normalized fluorescence is proportional to the photon count. (c) N-V energy-level diagram and room-temperature experimental apparatus. The N-V center in diamond exhibits spin-dependent fluorescence with triplet ground-state spin transitions. A flip mirror directs N-V fluorescence towards either a photodiode or a lock-in camera. An AWG generates MW pulses to control the N-V spin, rf signals for the microcoils, and frame triggers for camera exposure, utilizing its internal oscillator to synchronize the experiment. An SiC wafer serves as a mount for the MW loop, microcoils, and N-V-diamond chip. An rf test coil (not shown) provides signals for calibration of ac magnetometry.

APPENDIX B: DYNAMICAL-DECOUPLING-BASED ac MAGNETOMETRY

The negatively charged nitrogen-vacancy defect of interest has electronic spin $S = 1$, and its triplet ground state exhibits a zero-field splitting between the $|m_s = 0\rangle$ and $|m_s = \pm 1\rangle$ magnetic sublevels [Fig. 6(c)]. The application of a bias magnetic field further splits the degenerate $|m_s = \pm 1\rangle$ states via the Zeeman effect. We use a pair of ring magnets to apply a bias magnetic field of approximately 22 mT aligned along one of the four N-V orientations in the diamond crystal. In this bias magnetic field regime, the effects of the transverse diamond crystal strain and electric field can be neglected [37,38], such that the approximate Hamiltonian for the N-V ground state is given by [8,39,40]

$$\frac{\hat{H}}{\hbar} \approx (D + M_z)\hat{S}_z^2 + \frac{\gamma}{2\pi} B_z \hat{S}_z, \tag{B1}$$

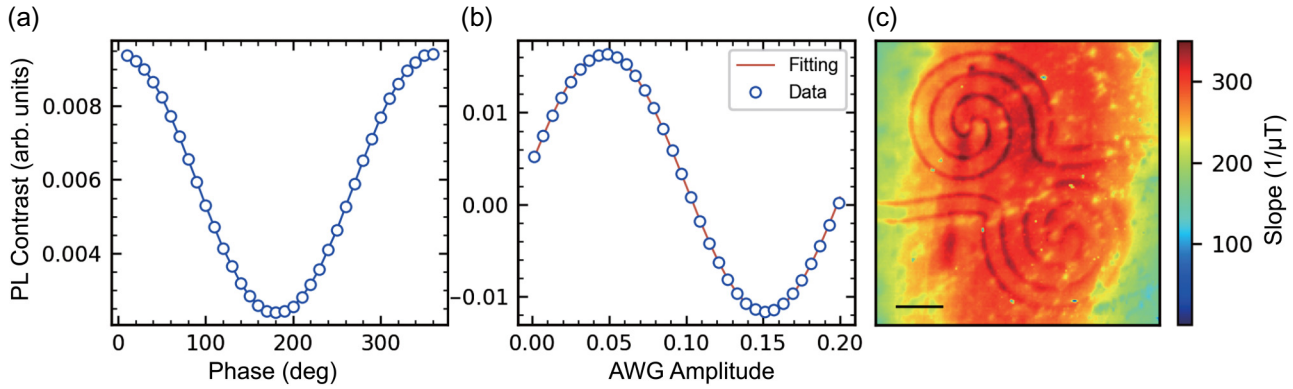


FIG. 7. Example calibration measurements with the rf QDM for dynamical-decoupling-based ac magnetometry (photodiode measurements with a laser beam illumination diameter of approximately 50 μm) and imaging (lock-in camera measurements). (a) Phase sweep of photodiode ac magnetometry to determine the initial phase of a nominally in-phase ac magnetic field (= 1 MHz), applied with the rf test coil. (b) Photodiode ac magnetometry curve of relative N-V photoluminescence contrast using the XY8-8 sequence, showing good agreement with a sinusoidal fit. (c) Imaged spatial distribution of the zero-crossing slope of the ac magnetometry curve, which exhibits a spatial dependence due to the laser beam illumination of the N-V layer; see Fig. 6(b). The scale bar corresponds to 50 μm.

where $\hat{S}_z$ is the dimensionless spin-1 operator along the N-V quantization axis, $\gamma = 2\pi \times 28.024$ GHz/T [15] is the N-V electronic gyromagnetic ratio, $D \approx 2.87$ GHz is the zero-field splitting at room temperature [15], B_z is the bias magnetic field, and M_z is the longitudinal component of the crystal stress.

The dynamical-decoupling-based protocol for ac magnetometry begins with an optical pulse to initialize the electronic spin state to $|m_s = 0\rangle$ for each N-V defect in the ensemble being probed. Subsequently, a $\pi/2$-MW pulse prepares each N-V defect in the ensemble in a superposition between $|m_s = 0\rangle$ and $|m_s = 1\rangle$ for ac magnetic field sensing. The ac signal to be detected is an oscillating magnetic field $B_{\rm ac} = B_z \cos(2\pi f_s t + \phi_0)$, where B_z is the projection of the magnetic field amplitude on the N-V axis, f_s is the oscillation frequency, and ϕ_0 is the phase offset between the applied ac field and the dynamical decoupling sequence. After N_π π pulses, each separated by a free precession time $\tau = 1/2f_s$, the dynamical phase accumulation by each N-V defect in the ensemble is given by

$$\theta(B_z, \phi_0) = \frac{g\mu_B N_\pi B_z}{\pi\hbar f_s}\cos\phi_0, \tag{B2}$$

where $g \approx 2$ is the Landé g factor, μ_B is the Bohr magneton, and $\hbar$ is the reduced Planck constant. With a $\pi/2$-phase difference between the first and last $\pi/2$ pulses in the sequence, the N-V fluorescence readout signal is given by

$$\begin{aligned} S(B_z, \phi_0) &= S_o + S_a \sin(\theta) \\ &= S_o + S_a \sin(\kappa B_z \cos\phi_0), \end{aligned} \tag{B3}$$

where S_o is the N-V fluorescence offset, S_a is the fluorescence oscillation amplitude, and $\kappa = g\mu_B N_\pi/\pi\hbar f_s$ is a constant. The N-V fluorescence readout corresponding to projection onto the $|m_s = 0\rangle$ and $|m_s = 1\rangle$ states are $S_o \pm S_a$, respectively.

We calibrate the rf QDM's performance of ac magnetometry as follows. We first adjust the phase ϕ_0 of a modest amplitude signal (= 1 MHz) applied to the rf test coil, by setting the AWG output amplitude to 0.01 (equivalent to 11.25 mV $V_{\rm pp}$ across the rf test coil). We then perform ac magnetometry as described above, using the photodiode to collect the N-V fluorescence with a laser beam illumination diameter of approximately 50 μm. The resulting N-V photoluminescence contrast can be approximated as $S(\phi_0) \approx S_o + S_a\kappa B_z \cos\phi_0$. By sweeping the phase offset ϕ_0, we determine the experimental phase shift for the ac test signal, as measured with the dynamical decoupling sequence, from the value of ϕ_0 that gives maximum N-V fluorescence contrast. As shown in Fig. 7(a), this experimental phase shift is very small (about 1°). Next, with the phase fixed at $\phi_0 = 0$, we sweep the AWG output amplitude (changing B_z over a range comparable to that observed in microcoil experiments) to determine the ac magnetometry curve [Fig. 7(b)]. After fitting with a sine function, we extract the AWG amplitude change $A_{2\pi}$ for 2π-phase accumulation by the N-V defects (i.e., $\theta = 2\pi$). Based on Eq. (B2), the ac magnetic field amplitude for 2π-phase accumulation $B_{2\pi}$ is given by $2\pi^2 f_s\hbar/g\mu_B N_\pi$. The calibration factor to convert the AWG amplitude to the ac magnetic field amplitude is then calculated as $C = B_{2\pi}/A_{2\pi}$. The derivative of the magnetometry curve at the zero-crossing point provides us with the slope of the N-V fluorescence signal varying with the AWG output amplitude, $\Delta S/\Delta A$. For ac magnetic sensing, the zero-crossing slope is given by $\Delta S/\Delta B_z = C\Delta S/\Delta A$. In the imaging modality, we perform this calibration process for each pixel. The spatial

distribution of the ac magnetometry curve zero-crossing slope, which is mainly determined by the laser beam illumination of the N-V layer, is shown in Fig. 7(c). Once an N-V fluorescence image is acquired, the in-phase ac magnetic field image can be extracted using the precalibrated zero-crossing slope for each pixel.

APPENDIX C: rf MAGNETIC IMAGING SPATIAL RESOLUTION AND FREQUENCY RANGE

To further illustrate the approximate 2-μm spatial resolution and easily tunable frequency range of the rf QDM, we perform experiments under the same conditions as those described in Fig. 2(b), except we use a diamond with a 1.7-μm surface N-V layer. We begin by applying an ac signal at 1 MHz, with a peak current of 6.6 μA, to the upper microcoil on the N-V-diamond surface. After a 1.2-s acquisition (200 camera external frames), we obtain an rf magnetic field amplitude image with a peak-to-peak difference of about 300 nT, revealing the near-field pattern generated by the upper microcoil with SNR ≈ 53, in good agreement with numerical simulation [Fig. 8]. The simulation is performed using the same approach described in Sec. III A, averaging the three-dimensional magnetic field from the microcoil at a 7-μm stand-off distance over the N-V layer thickness.

As mentioned in Sec. III A, the central detection frequency of the dynamical decoupling sequence is easily tunable over the megahertz scale. The maximum sequence length, limited by the spin decoherence time T_2 of the N-V ensemble, determines the lower limit of the signal detection frequency, f_s. For the XY8-8 sequence, $T_2 \approx 60$ μs [Fig. 10], resulting in $\tau \approx 1$ μs and hence a minimum $f_s \approx 0.5$ MHz. As a demonstration, we image the rf magnetic field generated by a 0.5-MHz ac signal applied to the upper microcoil, with the same peak current of 6.6 μA [Fig. 8]. Although the magnetic field pattern is consistent with the simulation and experiment at $f_s = 1$ MHz, the SNR decreases to approximately 34, due to N-V fluorescence signal decay with the longer sensing time. To perform imaging of even lower-frequency narrowband signals, the Hahn spin-echo sequence can be used [41]. For the diamonds used in the present experiment, this would allow a maximum $\tau = T_{2,\mathrm{Hahn}} \approx 10$ μs, indicating that the rf QDM is capable of imaging narrowband signals down to about 50 kHz, albeit with reduced sensitivity.

The maximum detection frequency of the dynamical decoupling sequence is limited by the length of the π pulses, which is determined by the N-V Rabi frequency of the MW driving. At present, the rf QDM's on-chip Ω-shaped coplanar waveguide achieves a 6.4-MHz Rabi frequency with the maximum output of the MW amplifier (approximately 50 dBm). Since τ must be longer than the π-pulse duration, the maximum detection frequency of the rf QDM is presently less than 6.4 MHz. As a demonstration, we image a 5-MHz rf magnetic field pattern, again for $I_p = 6.6$ μA, with SNR ≈ 47, similar to the results obtained at 1 MHz. A straightforward way to increase the Rabi frequency (and hence the maximum signal frequency that can be imaged) is by reducing the diameter of the MW antenna; however, this would worsen MW and hence Rabi frequency homogeneity, which is detrimental for wide-field imaging. Another option is to use resonators that provide a stronger Rabi frequency, but this approach fixes the detection frequency, limiting the versatility of the rf QDM. To allow imaging of higher signal frequencies (from about 10 MHz to the gigahertz range) without the limitations noted above, we plan in future work to investigate the use of a quantum frequency mixing protocol [34] with the rf QDM.

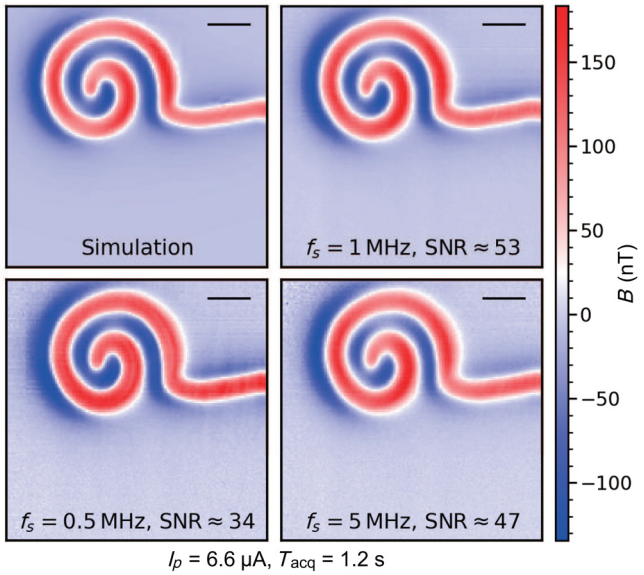


FIG. 8. rf QDM imaging of narrowband magnetic fields of known phase, using a dynamical decoupling (XY8-8) protocol and a 1.7-μm-thick N-V layer diamond. Alternating currents of 1, 0.5, and 5 MHz with $I_p = 6.6$ μA are applied to the upper microcoil, in separate experiments. After averaging over 1.2 s for each signal frequency, the experimental images exhibit SNRs of approximately 50, 34, and 47, respectively, calculated using the same method as for Fig. 2(b) in the main text. The imaged spatial patterns of rf magnetic fields are consistent over an order of magnitude of the signal frequency, and also with a numerical simulation of an applied dc signal at 6.6 μA. All scale bars correspond to 50 μm in this figure. The colorbar is not centered around zero because of asymmetry in the projection of the rf magnetic field amplitude on the sensing N-V axis.

APPENDIX D: FOURIER ANALYSIS OF THE CASR SIGNAL

For the CASR protocol, the phase offset of each readout is varying due to the signal being time dependent. Equation

(B3) can be rewritten as

$$\begin{aligned} S(t, B_z, \phi_0) &= S_o + S_a \sin[\kappa B_z \cos(2\pi f_s t + \phi_0)] \\ &= S_o + 2S_a \sum_{n=0}^{\infty} (-1)^n J_{2n+1}(\kappa B_z) \\ &\quad \times \cos[(2n+1)(2\pi f_s t + \phi_0)], \end{aligned} \tag{D1}$$

where $J_n(x)$ is the nth-order Bessel function and f_s is the signal central frequency. The CASR spectrum after an FFT is given by

$$\begin{aligned} S(f, B_z, \phi_0) &= \sqrt{2\pi}\Big(S_o \delta(f) + 2\pi S_a \sum_{n=0}^{\infty} (-1)^n J_{2n+1}(\kappa B_z) \\ &\quad \times \{e^{-i\phi_0}\delta[f - (2n+1)f_s] + e^{i\phi_0}\delta[f + (2n+1)f_s]\}\Big) \\ &= S_{\mathrm{dc}} + S_{\mathrm{Real}} + iS_{\mathrm{Imag}}, \end{aligned} \tag{D2}$$

where $\delta(f)$ is the Dirac function in frequency space, and S_{dc}, S_{Real}, and S_{Imag} are the dc component, real part, and imaginary part of the Fourier spectrum, respectively. Here $S_{\mathrm{dc}} = \sqrt{2\pi} S_o \delta(f)$, whereas the real and imaginary parts are given by

$$\begin{aligned} S_{\mathrm{Real}}(f, B_z, \phi_0) &= (2\pi)^{3/2} S_a \cos(\phi_0) \sum_{n=0}^{\infty} (-1)^n J_{2n+1}(\kappa B_z) \\ &\quad \times \{\delta[f + (2n+1)f_s] + \delta[f - (2n+1)f_s]\}, \\ S_{\mathrm{Imag}}(f, B_z, \phi_0) &= (2\pi)^{3/2} S_a \sin(\phi_0) \sum_{n=0}^{\infty} (-1)^n J_{2n+1}(\kappa B_z) \\ &\quad \times \{\delta[f + (2n+1)f_s] - \delta[f - (2n+1)f_s]\}. \end{aligned} \tag{D3}$$

In the rf QDM CASR experiments reported in Sec. III C, we utilize the XY8-8 sequence for imaging rf magnetic field patterns with $B_{z,\max} \approx 40$ nT, resulting in $\kappa B_{z,\max} \approx 0.8$. In the regime of $\kappa B_z < 1$, we can ignore the contribution of higher-order Bessel functions. Keeping the first-order Bessel term's positive part due to the symmetry of the Fourier spectrum, the real and imaginary parts can be simplified as

$$\begin{aligned} S^{+}_{\mathrm{Real}}(f, B_z, \phi_0) &= (2\pi)^{3/2} S_a \cos(\phi_0) J_1(\kappa B_z) \delta(f - f_s), \\ S^{+}_{\mathrm{Imag}}(f, B_z, \phi_0) &= -(2\pi)^{3/2} S_a \sin(\phi_0) J_1(\kappa B_z) \delta(f - f_s). \end{aligned} \tag{D4}$$

For rf QDM CASR experiments, the measurement separation is $t_m = N_d\, t_{\mathrm{Seq}}$, where t_{Seq} is the sequence length for one camera demodulation cycle. The camera frame rate $f_{\mathrm{SR}} = 1/t_m$. Based on the Nyquist-Shannon sampling theorem, the bandwidth of the measured Fourier spectrum is $f_{\mathrm{SR}}/2$. The CASR alias frequency is $f_a = |f_s - m f_{\mathrm{SR}}|$, where m is the integer closest to f_s/f_{SR}. Consequently, for each pixel in a CASR image, the measured signal components are

$$\begin{aligned} S^{+}_{\mathrm{Real},m}(f, B_z, \phi_0) &= (2\pi)^{3/2} S_a \cos(\phi_0) J_1(\kappa B_z) \delta(f - f_a), \\ S^{+}_{\mathrm{Imag},m}(f, B_z, \phi_0) &= -(2\pi)^{3/2} S_a \sin(\phi_0) J_1(\kappa B_z) \delta(f - f_a). \end{aligned} \tag{D5}$$

Here, we define the amplitude to have the same sign as the real component; thus, the FFT spectrum amplitude of a measured rf magnetic field is given by

$$\begin{aligned} S^{+}_{\mathrm{Amp},m}(f, B_z) &= \frac{S^{+}_{\mathrm{Real},m}}{|\, S^{+}_{\mathrm{Real},m}\,|} \sqrt{{S^{+}_{\mathrm{Real},m}}^2 + {S^{+}_{\mathrm{Imag},m}}^2} \\ &= (2\pi)^{3/2} S_a J_1(\kappa B_z) \delta(f - f_a). \end{aligned} \tag{D6}$$

By integrating the relevant peak of the FFT spectrum, the CASR signal at each frequency component is

$$\begin{aligned} S_{\mathrm{CASR}}(B_z) &= \int_{f_a - \Delta f}^{f_a + \Delta f} S^{+}_{\mathrm{Amp},m}(f, B_z)\, df \\ &= (2\pi)^{3/2} S_a J_1(\kappa B_z). \end{aligned} \tag{D7}$$

In our experiment, the peak half linewidth $\Delta f \approx 1$ Hz, resulting in $S_{\mathrm{CASR}} \approx S^{+}_{\mathrm{Amp},m}$. When $\kappa B_z < 1$, the first-order Bessel function closely approximates a linear function, giving $S_{\mathrm{CASR}} \propto B_z$. In the imaging modality, the N-V fluorescence signal amplitude S_a has a spatial distribution due to the laser beam shape. Thus, we normalize the FFT image with the N-V fluorescence image [Fig. 6(b)] to obtain the final CASR image of the rf magnetic field amplitude.

For a CASR phase image, we calculate the rf magnetic field phase offset for each pixel using the real and imaginary components of the Fourier spectrum, given by Eqs. (D5), as follows:

$$\phi_0 = \arctan\left(-S^{+}_{\mathrm{Imag},m} / S^{+}_{\mathrm{Real},m}\right). \tag{D8}$$

We then construct CASR phase images at each alias frequency within the spectral bandwidth.

APPENDIX E: CASR IMAGING EXPERIMENTAL DETAILS

As noted in Sec. III C, CASR imaging data are acquired with a 500-Hz frame rate for a 1-s measurement. To improve the image SNR, we perform a 1-s background measurement (with no rf signal applied to the microcoils) after each CASR image acquisition (with signal applied), and repeat 100 times for signal averaging. During the imaging process, the camera saves 500 external frames in its RAM, transfers it to the computer, and clears the buffer to start the next iteration of the experiment. The total

measurement time is 200 s; however, because of the data transfer time, the wall time for the experiment is approximately 30 min. The total data size is large (17 GB), but after background subtraction and averaging the CASR signal is in the time domain for each pixel, resulting in a $150 \times 150 \times 500$ matrix, with a data size of only 80 MB. The computational time of the Fourier transformation for all pixels across the FOV is 0.4 s.

The current implemented generation of Heliotes cameras is unable to read and write data simultaneously. Instead, it temporarily stores the measurement data in its memory buffer. Once the buffer is nearly full, it pauses the experiment to transfer the data to the computer and clear the buffer, which takes approximately 5 s. This limitation could be addressed by using cameras capable of directly saving data to the computer, which would significantly improve performance for practical applications of the rf QDM.

In the main text, we show CASR images at each applied rf signal frequency component (tone), and also at alias frequencies far from any signal tone [Fig. 4(a)]. In Fig. 9(a), we provide complementary CASR amplitude images, for the same experimental parameters, at alias frequencies with a small offset (1 Hz) from the signal tones at 65 and 125 Hz, and at an intermediate alias frequency (95 Hz). The colorbar range is set 20 times smaller than in Fig. 4(a) to visualize the weak signal amplitudes when detuned even by 1 Hz from the applied signal tones. In Fig. 9(b), we show $S^{+}_{\mathrm{Real},m}$ and $-S^{+}_{\mathrm{Imag},m}$ as a function of the alias frequency for the three test pixels $P_{1,2,3}$. These results complement the polar plot of Fig. 4(d), which depicts the phase offsets and peak values of the real and imaginary components of the CASR spectrum for each signal frequency component. The phase error in our CASR measurements is estimated as

$$\delta\phi = \arcsin\left(\frac{\sigma_1}{S_{\mathrm{CASR}}(f_2)}\right) \approx 0.6^{\circ}, \tag{E1}$$

where σ_1 is the noise floor of the CASR spectrum of the test pixel P_1 in Fig. 4(b), and $S_{\mathrm{CASR}}(f_2)$ is the CASR amplitude of the alias frequency at $f_2 = 125$ Hz.

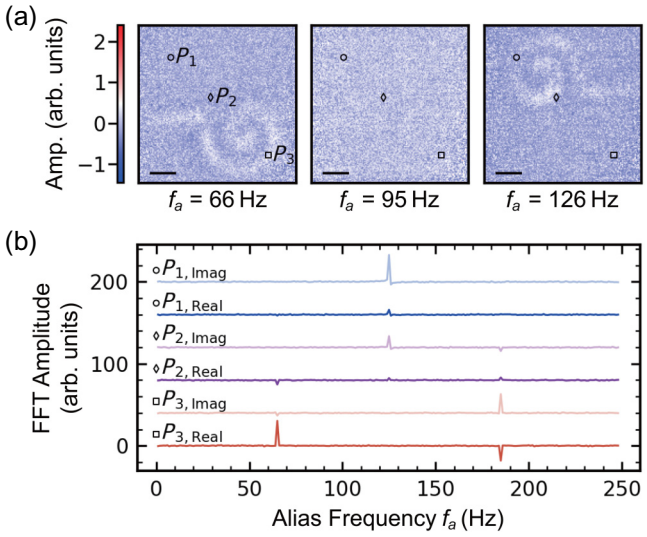


FIG. 9. (a) CASR images of rf magnetic field amplitudes for the same experimental parameters as in Fig. 4, with alias frequency values of 66 and 126 Hz, offset by 1 Hz from the applied signal frequency components (tones) at 65 and 125 Hz, respectively, and at an intermediate alias frequency of 95 Hz. All scale bars correspond to 50 μm. The colorbar is not centered around zero because of asymmetry in the projection of the rf magnetic field amplitude on the sensing N-V axis. (b) Real and imaginary components of the CASR spectrum, as a function of the alias frequency, at three test pixels $P_{1,2,3}$ with positions labeled in (a). Peaks corresponding to the three applied signal frequency components (tones) are illustrated in the phase offset polar plot in Fig. 4(d).

APPENDIX F: ac MAGNETIC SENSITIVITY OPTIMIZATION

For an ac magnetic field measurement by an N-V sensor using a dynamical decoupling sequence, the magnetic sensitivity limited by photon shot noise and spin projection noise is approximately given by [2]

$$\eta_{\mathrm{ac}} = \frac{\pi}{2\Delta m_s \gamma} \frac{1}{Ce^{(-t_{\mathrm{S}}/T_2)^p}\sqrt{N}} \frac{\sqrt{t_{\mathrm{I,R}} + t_{\mathrm{S}}}}{t_{\mathrm{S}}}, \tag{F1}$$

where $\Delta m_s = 1$ accounts for the difference in the m_s states used for sensing, C is the optical measurement contrast at sensing time $t_{\mathrm{S}} = 0$, T_2 is the N-V spin coherence time, p describes the N-V spin coherence envelope decay shape [42], N is the average photon number collected per measurement, and $t_{\mathrm{I,R}}$ is the combined initialization and readout time during the dynamical decoupling sequence. The spin coherence time measured with dynamical decoupling sequences scales with a power law as a function of the number of π pulses [43], $T_2(N_\pi) = T_2(1)N_\pi{}^s$, where s is determined by the noise spectrum of the decohering spin bath and typically exhibits sublinear behavior [44]. For a given ac signal at frequency f_s, the sensing time has a linear dependence on the π-pulse number $t_{\mathrm{S}} = 2N_\pi/f_s$. After experimental adjustment of C, N, and $t_{\mathrm{I,R}}$, the ac sensitivity is optimized with a specific number of pulses [2]:

$$N_{\pi,\mathrm{opt}} = \left[\frac{[2f_s T_2(1)]^p}{2p(1-s)}\right]^{1/p(1-s)}. \tag{F2}$$

In photodiode measurements with the 10-μm N-V layer diamond, we determine a typical, spatially averaged value of $T_2(1) = 10$ μs using a Hahn spin-echo sequence [45]

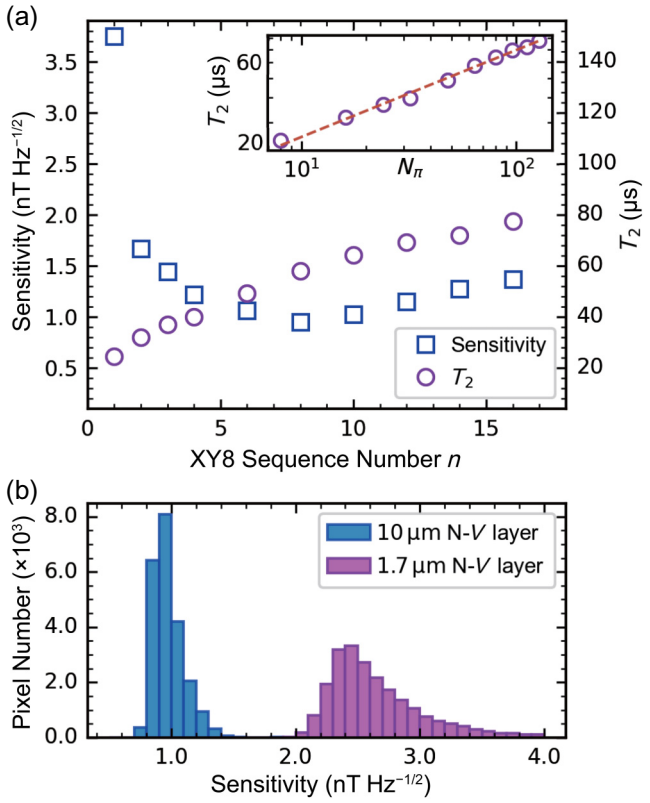


FIG. 10. (a) ac magnetic sensitivity optimization with varying XY8 sequence number, performed with photodiode measurements of the 10-μm N-V layer diamond. As the XY8-n sequence number increases, the N-V spin coherence time T_2 increases. The optimized median single-pixel sensitivity across the FOV is achieved with the XY8-8 sequence. The inset illustrates the fitting of the measured coherence time T_2 with π-pulse number $N_\pi = 8n$, showing a power law. The fitted slope $s = 0.44(1)$. (b) rf QDM imaging using the lock-in camera and a 1-MHz signal applied with the rf test coil. Histogram showing the distribution of single-pixel ac sensitivity across the FOV using the XY8-8 sequence. The median sensitivity is 0.93(1) nT Hz$^{-1/2}$ for the 10-μm-thick N-V layer diamond, and 2.56(1) nT Hz$^{-1/2}$ for the 1.7-μm-thick N-V layer diamond.

and $p = 1.3$. By fitting the measured coherence time variation with pulse number, we derive a value of $s = 0.44(1)$ [inset of Fig. 10(a)]. Using these parameters, for $f_s = 1$ MHz, we estimate $N_{\pi,\mathrm{opt}}/8$ to be approximately 16, indicating that the XY8-16 sequence provides optimized sensitivity. However, during rf QDM magnetic field imaging with the lock-in camera, the contribution of camera quantization noise to ac magnetic sensitivity must also be considered. With a fixed number of demodulation cycles, camera noise increases with sensing sequence length, as shown in Appendix G. Considering both shot noise and camera noise, the optimized sensing sequence should be shorter than the XY8-16 sequence.

To ascertain the optimal sensing sequence including camera noise, we vary the number of XY8 sequences and measure the ac sensitivity of each pixel across the FOV. The experimental per-pixel magnetic sensitivity results are computed from $\eta = \delta B\sqrt{T_{\mathrm{acq}}}$, where δB is the smallest magnetic field that can be measured with SNR = 1 after acquisition time T_{acq}. For a camera operating at an external frame rate f_{SR}, a series of magnetic noise images are collected. Then the magnetic noise of each pixel, σ_{pxl}, is obtained from the standard deviation of the magnetometry data from that pixel across all recorded frames. The measured per-pixel magnetic sensitivity is then given by

$$\eta = \frac{\sigma_{\mathrm{pxl}}}{\sqrt{f_{\mathrm{SR}}}}. \tag{F3}$$

The results displayed in Fig. 10(a) are obtained using 500 frames collected for $f_{\mathrm{SR}} = 1/[4N_d(t_{\mathrm{I,R}} + t_{\mathrm{S}})]$, where the demodulation cycle number $N_d = 34$, $t_{\mathrm{I,R}} = 26$ μs, $t_{\mathrm{S}} = N_\pi/(2f_s)$, and the signal frequency $f_s = 1$ MHz (applied with the rf test coil). The optimized sequence is determined to be the XY8-8 sequence, with a median per-pixel ac sensitivity of 0.93(1) nT Hz$^{-1/2}$. Given the sensing voxel volume of 40 μm^3, we calculate a volume-normalized ac sensitivity of 5.88 nT Hz$^{-1/2}$ μm$^{3/2}$, which is comparable to state-of-the-art photodiode-based XY8 sensitivity for ac magnetometry using N-V ensembles [19]. We also perform an analogous characterization and ac magnetometry optimization for the 1.7-μm-thick N-V layer diamond with similar results. In particular, we determine a median per-pixel ac sensitivity of 2.56(1) nT Hz$^{-1/2}$ at the same experimental condition [Fig. 10(b)]. The volume-normalized ac sensitivity is calculated to be 6.68 nT Hz$^{-1/2}$ μm$^{3/2}$, which is slightly worse than for the 10-μm N-V layer diamond. The reason for this difference is that the camera quantization noise (discussed in Appendix G) is larger for the 1.7-μm N-V layer diamond, due to this diamond's fewer number of N-V centers in the thinner layer, resulting in a lower total N-V fluorescence rate per imaging pixel, and hence a reduced magnetometry slope.

APPENDIX G: NOISE SOURCE ANALYSIS

For the rf QDM measurements presented here, photon shot noise and camera quantization noise are the major limitations to ac magnetic sensitivity. We estimate shot-noise-limited ac sensitivity using Eq. (F1). By focusing the N-V fluorescence with a laser beam illumination diameter of approximately 50 μm onto a photodiode, we experimentally determine typical N-V-ensemble-averaged XY8-8 parameters for the 10-μm N-V layer diamond to be about $C = 3\%$, $T_2 = 58$ μs, and $p = 1.3$. As mentioned in the previous section, we use $t_{\mathrm{I,R}} = 26$ μs and $t_{\mathrm{S}} = 8 \times 8 \times 0.5 = 32$ μs for a XY8-8 rf QDM magnetic imaging experiment, and estimate that $N = 4 \times 10^4$ photons are collected in a single camera pixel [8]. With these

values, the estimated photon shot-noise-limited per-pixel ac magnetic sensitivity for a 1-MHz signal frequency is $\eta_{\text{shot}} = 0.3\ \text{nT}\,\text{Hz}^{-1/2}$.

The quantization noise of the Heliotis lock-in camera includes electronic and digitization noise. For each external frame, the standard deviation of the noise is dependent on the number of demodulation cycles (N_d) spent accumulating differences between successive internal exposures, and can be estimated in the camera device unit (DU) as [46]

$$\sigma_{\text{quant}} = \sqrt{0.81 + 0.16N_d}. \tag{G1}$$

To convert the DU estimate of quantization noise to equivalent magnetic noise, we calculate the median zero-crossing slope of imaged ac magnetometry curves across the whole FOV [Fig. 7(c)] and find that $\overline{\Delta S/\Delta B_z} = 258\ \text{DU}/\mu\text{T}$. The estimated quantization-noise-limited per-pixel ac magnetic sensitivity is given by

$$\eta_{\text{quant}} = \frac{\sigma_{\text{quant}}}{\overline{\Delta S/\Delta B_z}\sqrt{f_{\text{SR}}}}, \tag{G2}$$

which is about $0.86\ \text{nT}\,\text{Hz}^{-1/2}$ for the rf QDM using the 10-μm N-V layer diamond. In the process of optimizing camera quantization noise, increasing the demodulation cycle number N_d leads to a larger σ_{quant} and a smaller sample rate f_{SR}. However, when operating in the regime where the photon count for each pixel does not saturate the well depth of the camera, the magnetometry slope $\overline{\Delta S/\Delta B_z}$ increases linearly with N_d, leading to less quantization noise. Experimentally, we sweep the demodulation cycle number N_d and observe a linear region for $N_d \leqslant 34$. Then, we use the maximum N_d to utilize the full digitizer range of the camera in the experiment. After adding photon shot noise and camera quantization noise in quadrature, the combined estimate of per-pixel ac magnetic sensitivity is $\eta_{\text{est}} = \sqrt{\eta_{\text{shot}}^2 + \eta_{\text{quant}}^2} = 0.91\ \text{nT}\,\text{Hz}^{-1/2}$, which is consistent with the measured median per-pixel magnetic sensitivity of $0.93(1)\ \text{nT}\,\text{Hz}^{-1/2}$.

For the present rf QDM, the ac magnetic field sensitivity is limited by the Heliotis lock-in camera. The dynamic range of the Heliotis camera is fixed (DU from 0 to 1023, 10 bits), and the camera sensor is optimized for unity gain [46]. For a given number of demodulation cycles N_d, the quantization noise remains constant. Thus, enhancing the median zero-crossing slope of imaged ac magnetometry curves, which is utilized for converting the camera external frame output from DU to a magnetic field value, can effectively decrease the magnetic noise contribution from quantization noise. The slope of an ac magnetometry curve for a given N_d is directly proportional to both N-V fluorescence intensity and spin-state readout contrast, factors that influence the accumulated differential photon number ΔN in a camera external frame. Moreover, the slope also depends on the N-V spin coherence time T_2. Consequently, rf QDM sensitivity will benefit from efforts to increase N-V fluorescence intensity, spin-state readout contrast, and T_2, as well as diamond engineering efforts to enable increased laser illumination intensity while mitigating contrast degradation due to N-V charge-state conversion [47].

We note an alternative approach for wide-field N-V-diamond measurements using an array of single-photon avalanche diodes (SPADs) [48]. The SPAD array provides single-photon counting capability and high time resolution (frame rate up to 100 kHz). However, it is only applicable to low photon counts, with correspondingly greatly reduced magnetic field sensitivity per pixel compared to a camera-based QDM. The SPAD array is thus best suited for very-thin (< 100 nm) N-V layers with a single or a few N-V centers per pixel.

[1] J. M. Taylor, P. Cappellaro, L. Childress, L. Jiang, D. Budker, P. R. Hemmer, A. Yacoby, R. Walsworth, and M. D. Lukin, High-sensitivity diamond magnetometer with nanoscale resolution, Nat. Phys. **4**, 810 (2008).

[2] J. F. Barry, J. M. Schloss, E. Bauch, M. J. Turner, C. A. Hart, L. M. Pham, and R. L. Walsworth, Sensitivity optimization for NV-diamond magnetometry, Rev. Mod. Phys. **92**, 015004 (2020).

[3] E. V. Levine, M. J. Turner, P. Kehayias, C. A. Hart, N. Langellier, R. Trubko, D. R. Glenn, R. R. Fu, and R. L. Walsworth, Principles and techniques of the quantum diamond microscope, Nanophotonics **8**, 1945 (2019).

[4] S. J. Devience, L. M. Pham, I. Lovchinsky, A. O. Sushkov, N. Bar-Gill, C. Belthangady, F. Casola, M. Corbett, H. Zhang, M. Lukin, H. Park, A. Yacoby, and R. L. Walsworth, Nanoscale NMR spectroscopy and imaging of multiple nuclear species, Nat. Nanotechnol. **10**, 129 (2015).

[5] S. Dasika, M. Parashar, and K. Saha, Mapping AC susceptibility with quantum diamond microscope, Rev. Sci. Instrum. **94**, 053702 (2023).

[6] G. Chatzidrosos, A. Wickenbrock, L. Bougas, H. Zheng, O. Tretiak, Y. Yang, and D. Budker, Eddy-current imaging with nitrogen-vacancy centers in diamond, Phys. Rev. Appl. **11**, 014060 (2019).

[7] K. Mizuno, H. Ishiwata, Y. Masuyama, T. Iwasaki, and M. Hatano, Simultaneous wide-field imaging of phase and magnitude of AC magnetic signal using diamond quantum magnetometry, Sci. Rep. **10**, 11611 (2020).

[8] J. Tang, Z. Yin, C. A. Hart, J. W. Blanchard, J. T. Oon, S. Bhalerao, J. M. Schloss, M. J. Turner, and R. L. Walsworth, Quantum diamond microscope for dynamic imaging of magnetic fields, AVS Quantum Sci. **5**, 044403 (2023).

[9] D. R. Glenn, D. B. Bucher, J. Lee, M. D. Lukin, H. Park, and R. L. Walsworth, High-resolution magnetic resonance spectroscopy using a solid-state spin sensor, Nature **555**, 351 (2018).

[10] P. V. Klimov, A. L. Falk, D. J. Christle, V. V. Dobrovitski, and D. D. Awschalom, Quantum entanglement at ambient

conditions in a macroscopic solid-state spin ensemble, Sci. Adv. **1**, e1501015 (2015).

[11] M. Widmann, S. Y. Lee, T. Rendler, N. T. Son, H. Fedder, S. Paik, L. P. Yang, N. Zhao, S. Yang, I. Booker, A. Denisenko, M. Jamali, S. A. Momenzadeh, I. Gerhardt, T. Ohshima, A. Gali, E. Janzén, and J. Wrachtrup, Coherent control of single spins in silicon carbide at room temperature, Nat. Mater. **14**, 164 (2015).

[12] Z. Jiang, H. Cai, R. Cernansky, X. Liu, and W. Gao, Quantum sensing of radio-frequency signal with Nv centers in SiC, Sci. Adv. **9**, eadg2080 (2023).

[13] A. Gottscholl, M. Kianinia, V. Soltamov, S. Orlinskii, G. Mamin, C. Bradac, C. Kasper, K. Krambrock, A. Sperlich, M. Toth, I. Aharonovich, and V. Dyakonov, Initialization and read-out of intrinsic spin defects in a van der Waals crystal at room temperature, Nat. Mater. **19**, 540 (2020).

[14] R. Rizzato, M. Schalk, S. Mohr, J. C. Hermann, J. P. Leibold, F. Bruckmaier, G. Salvitti, C. Qian, P. Ji, G. V. Astakhov, U. Kentsch, M. Helm, A. V. Stier, J. J. Finley, and D. B. Bucher, Extending the coherence of spin defects in hBN enables advanced qubit control and quantum sensing, Nat. Commun. **14**, 5089 (2023).

[15] V. M. Acosta, E. Bauch, M. P. Ledbetter, A. Waxman, L. S. Bouchard, and D. Budker, Temperature dependence of the nitrogen-vacancy magnetic resonance in diamond, Phys. Rev. Lett. **104**, 070801 (2010).

[16] Łukasz Cywiński, R. M. Lutchyn, C. P. Nave, and S. D. Sarma, How to enhance dephasing time in superconducting qubits, Phys. Rev. B **77**, 174509 (2008).

[17] COMSOL Multiphysics® v. 6.0, http://www.comsol.com/products/multiphysics/, 2021.

[18] N. R. Reed, D. Bhutto, M. J. Turner, D. M. Daly, S. M. Oliver, J. Tang, K. S. Olsson, N. Langellier, M. J. H. Ku, M. S. Rosen, and R. L. Walsworth, Machine learning for improved current density reconstruction from 2D vector magnetic images, arXiv:2407.14553.

[19] N. Arunkumar, K. S. Olsson, J. T. Oon, C. A. Hart, D. B. Bucher, D. R. Glenn, M. D. Lukin, H. Park, D. Ham, and R. L. Walsworth, Quantum logic enhanced sensing in solid-state spin ensembles, Phys. Rev. Lett. **131**, 100801 (2023).

[20] D. B. Bucher, D. R. Glenn, H. Park, M. D. Lukin, and R. L. Walsworth, Hyperpolarization-enhanced NMR spectroscopy with femtomole sensitivity using quantum defects in diamond, Phys. Rev. X **10**, 021053 (2020).

[21] N. Arunkumar, D. B. Bucher, M. J. Turner, P. TomHon, D. Glenn, S. Lehmkuhl, M. D. Lukin, H. Park, M. S. Rosen, T. Theis, and R. L. Walsworth, Micron-scale NV-NMR spectroscopy with signal amplification by reversible exchange, PRX Quantum **2**, 010305 (2021).

[22] K. D. Briegel, N. R. V. Grafenstein, J. C. Draeger, P. Blümler, R. D. Allert, and D. B. Bucher, Optical widefield nuclear magnetic resonance microscopy, arXiv:2402.18239.

[23] K. Arai, C. Belthangady, H. Zhang, N. Bar-Gill, S. J. DeVience, P. Cappellaro, A. Yacoby, and R. L. Walsworth, Fourier magnetic imaging with nanoscale resolution and compressed sensing speed-up using electronic spins in diamond, Nat. Nanotechnol. **10**, 859 (2015).

[24] H. Zhang, K. Arai, C. Belthangady, J. C. Jaskula, and R. L. Walsworth, Selective addressing of solid-state spins at the nanoscale via magnetic resonance frequency encoding, npj Quantum Inf. **3**, 31 (2017).

[25] X.-Y. Zhang, Y.-X. Wang, T. A. Tartaglia, T. Ding, M. J. Gray, K. S. Burch, F. Tafti, and B. B. Zhou, ac susceptometry of 2D van der Waals magnets enabled by the coherent control of quantum sensors, PRX Quantum **2**, 030352 (2021).

[26] C. Wang, M. Fan, B. Cao, B. Ye, and W. Li, Novel noncontact eddy current measurement of electrical conductivity, IEEE Sens. J. **18**, 9352 (2018).

[27] S. M. Oliver, D. J. Martynowych, M. J. Turner, D. A. Hopper, R. L. Walsworth, and E. V. Levine, in *ISTFA 2021: Conference Proceedings from the 47th International Symposium for Testing and Failure Analysis* (2021), pp. 96–107.

[28] P. Kehayias, J. Walraven, A. L. Rodarte, and A. M. Mounce, High-resolution short-circuit fault localization in a multilayer integrated circuit using a quantum diamond microscope, Phys. Rev. Appl. **20**, 014036 (2023).

[29] M. Ashok, M. J. Turner, R. L. Walsworth, E. V. Levine, and A. P. Chandrakasan, Hardware Trojan detection using unsupervised deep learning on quantum diamond microscope magnetic field images, J. Emerg. Technol. Comput. Syst. **18**, 1 (2022).

[30] M. J. Turner, N. Langellier, R. Bainbridge, D. Walters, S. Meesala, T. M. Babinec, P. Kehayias, A. Yacoby, E. Hu, M. Lončar, R. L. Walsworth, and E. V. Levine, Magnetic field fingerprinting of integrated-circuit activity with a quantum diamond microscope, Phys. Rev. Appl. **14**, 014097 (2020).

[31] P. Kehayias, E. V. Levine, L. Basso, J. Henshaw, M. Saleh Ziabari, M. Titze, R. Haltli, J. Okoro, D. R. Tibbetts, D. M. Udoni, E. Bielejec, M. P. Lilly, T.-M. Lu, P. D. D. Schwindt, and A. M. Mounce, Measurement and simulation of the magnetic fields from a 555 timer integrated circuit using a quantum diamond microscope and finite-element analysis, Phys. Rev. Appl. **17**, 014021 (2022).

[32] R. Bounik, F. Cardes, H. Ulusan, M. M. Modena, and A. Hierlemann, Impedance imaging of cells and tissues: Design and applications, BME Frontiers **2022**, 9857485 (2022).

[33] J. M. Schloss, J. F. Barry, M. J. Turner, and R. L. Walsworth, Simultaneous broadband vector magnetometry using solid-state spins, Phys. Rev. Appl. **10**, 034044 (2018).

[34] G. Wang, Y. X. Liu, J. M. Schloss, S. T. Alsid, D. A. Braje, and P. Cappellaro, Sensing of arbitrary-frequency fields using a quantum mixer, Phys. Rev. X **12**, 021061 (2022).

[35] H. Zhou, J. Choi, S. Choi, R. Landig, A. M. Douglas, J. Isoya, F. Jelezko, S. Onoda, H. Sumiya, P. Cappellaro, H. S. Knowles, H. Park, and M. D. Lukin, Quantum metrology with strongly interacting spin systems, Phys. Rev. X **10**, 031003 (2020).

[36] J. Choi, H. Zhou, H. S. Knowles, R. Landig, S. Choi, and M. D. Lukin, Robust dynamic Hamiltonian engineering of many-body spin systems, Phys. Rev. X **10**, 031002 (2020).

[37] P. Kehayias, M. J. Turner, R. Trubko, J. M. Schloss, C. A. Hart, M. Wesson, D. R. Glenn, and R. L. Walsworth, Imaging crystal stress in diamond using ensembles of nitrogen-vacancy centers, Phys. Rev. B **100**, 174103 (2019).

[38] A. Barfuss, M. Kasperczyk, J. Kölbl, and P. Maletinsky, Spin-stress and spin-strain coupling in diamond-based hybrid spin oscillator systems, Phys. Rev. B **99**, 174102 (2019).

[39] M. W. Doherty, N. B. Manson, P. Delaney, F. Jelezko, J. Wrachtrup, and L. C. Hollenberg, The nitrogen-vacancy colour centre in diamond, Phys. Rep. **528**, 1 (2013).

[40] C. A. Hart, J. M. Schloss, M. J. Turner, P. J. Scheidegger, E. Bauch, and R. L. Walsworth, N-*V*-diamond magnetic microscopy using a double quantum 4-Ramsey protocol, Phys. Rev. Appl. **15**, 044020 (2021).

[41] L. M. Pham, D. L. Sage, P. L. Stanwix, T. K. Yeung, D. Glenn, A. Trifonov, P. Cappellaro, P. R. Hemmer, M. D. Lukin, H. Park, A. Yacoby, and R. L. Walsworth, Magnetic field imaging with nitrogen-vacancy ensembles, New J. Phys. **13**, 045021 (2011).

[42] E. Bauch, S. Singh, J. Lee, C. A. Hart, J. M. Schloss, M. J. Turner, J. F. Barry, L. M. Pham, N. Bar-Gill, S. F. Yelin, and R. L. Walsworth, Decoherence of ensembles of nitrogen-vacancy centers in diamond, Phys. Rev. B **102**, 134210 (2020).

[43] L. M. Pham, N. Bar-Gill, C. Belthangady, D. Le Sage, P. Cappellaro, M. D. Lukin, A. Yacoby, and R. L. Walsworth, Enhanced solid-state multispin metrology using dynamical decoupling, Phys. Rev. B **86**, 045214 (2012).

[44] R. de Sousa, in *Electron spin resonance and related phenomena in low-dimensional structures* (Springer Berlin Heidelberg, Berlin, 2009), Vol. 1, p. 183.

[45] E. L. Hahn, Spin echoes, Phys. Rev. **80**, 580 (1950).

[46] Heliotis AG heliCam™ C3 Lock-in Camera, https://www.heliotis.com/en/sensors/lock-in-camera/, 2023.

[47] A. M. Edmonds, C. A. Hart, M. J. Turner, P.-O. Colard, J. M. Schloss, K. S. Olsson, R. Trubko, M. L. Markham, A. Rathmill, B. Horne-Smith, *et al.*, Characterisation of CVD diamond with high concentrations of nitrogen for magnetic-field sensing applications, Mater. Quantum Technol. **1**, 025001 (2021).

[48] G. Wang, F. Madonini, B. Li, C. Li, J. Xiang, F. Villa, and P. Cappellaro, Fast wide-field quantum sensor based on solid-state spins integrated with a SPAD array, Adv. Quantum Technol. **6**, 2300046 (2023).